Lithosphere

Research Article

Full Scale of Pore-Throat Size Distribution and Its Control on Petrophysical Properties of the Shanxi Formation Tight Sandstone Reservoir in the North Ordos Basin, China

Kai Liu,[1] Ren Wang,[1] Wanzhong Shi,[1] Juan Diego Martín-Martín,[2] Rong Qi,[3] Wei Zhang,[3] Shuo Qin,[1] and Anna Travé[2]

[1]*Key Laboratory of Tectonics and Petroleum Resources, Ministry of Education, China University of Geosciences, Wuhan 430074, China*
[2]*Departament de Mineralogia, Petrologia i Geologia Aplicada, Facultat de Ciències de la Terra, Universitat de Barcelona (UB), Barcelona 08028, Spain*
[3]*Exploration and Development Research Institute, SINOPEC North China Company, Zhengzhou 450006, China*

Correspondence should be addressed to Ren Wang; rwang@cug.edu.cn

Pore-throat size distribution is a key factor controlling the storage capacity and percolation potential of the tight sandstone reservoirs. However, the complexity and strong heterogeneity make it difficult to investigate the pore structure of tight sandstone reservoirs by using conventional methods. In this study, integrated methods of casting thin section, scanning electron microscopy, high-pressure mercury intrusion (HPMI), and constant-pressure mercury intrusion (CPMI) were conducted to study the pore-throat size distribution and its effect on petrophysical properties of the Shanxi Formation tight sandstones in the northern Ordos Basin (China). Results show that pore types of the Shanxi tight sandstone reservoirs include intergranular pores, dissolution pores, intercrystalline micropores, and microfracture, while the throats are dominated by sheet-like and tube-shaped throats. The HPMI-derived pore-throat size ranges from 0.006 to 10 μm, and the pore-throats with a radius larger than 10 μm were less frequent. The pore body size obtained from CPMI shows similar characteristics with radii ranging from 100 to 525 μm, while the throat size varies greatly with radii ranging from 0.5 to 11.5 μm, resulting in a wide range of pore-throat radius ratio. The full range of pore size distribution curves obtained from the combination of HPMI and CPMI displays multimodal with radii ranging from 0.006 to 525 μm. Permeability of the tight sandstone reservoirs is primarily controlled by relatively larger pore throats with small proportions, and the permeability decreases as the proportions of smaller pore-throats increase. The pervading nanopores in the tight gas sandstone reservoirs contribute little to the permeability but play an important role in the reservoir storage capacity. A new empirical equation obtained by multiple regression indicates that r_{15} (pore-throat size corresponding to 15% mercury saturation) is the best permeability estimator for tight gas sandstone reservoirs, which yields the highest correlation coefficient of 0.9629 with permeability and porosity.

1. Introduction

Tight sandstone gas is considered as a promising unconventional petroleum resource because of its tremendous reserves and relatively lower mining costs in China [1, 2]. In recent years, several big tight gas fields have been found in the Ordos Basin, Sichuan Basin, Songliao Basin, and Tarim Basin with an annual production of more than 222.5 $\times 10^8$ m³, making significant contributions to the oil and gas supply in China [3–5]. However, the tight sandstone reservoirs are characterized by complex pore network, poor reservoir

quality, and complicated oiliness, making the exploration and development of tight gas resource more challenging [6]. Reservoir quality, as a crucial factor and critical concern for tight gas exploration, is primarily controlled by the pore structure in the tight sandstone reservoirs [7–9]. Pore structure characteristics, including type, shape, size distribution, and connectivity of pore and throat, play a significant role in the petrophysical properties, the storage and seepage capacity, and oil and gas recovery of tight sandstone reservoirs [8, 10–13]. Pore-throat characteristics in the tight sandstone reservoir vary as a function of the depositional environment and complicated diagenetic alterations [14–16]. Sandstones with greater grain size and better sorting generally have greater primary porosity and better compressibility. Compaction and cements (e.g., carbonate and quartz cements) are usually responsible for the significant loss of primary intergranular pores, while the dissolution creates numerous secondary pores [17–19]. Clay minerals with various occurrences further complicate the pore-throat network by filling pores and producing substantial microscopic pores [20]. Therefore, the characterization of full-scaled pore-throat size of the tight sandstone reservoirs is difficult and challenging because of various pore types, wide pore-throat size distribution, and a significant proportion of nanoscale and microscale pore throats with poor connectivity [21–23].

Currently, commonly used techniques for investigating the pore structure of tight sandstones mainly include casting thin section, scanning electron microscopy (SEM), high-pressure mercury intrusion (HPMI), constant-pressure mercury intrusion (CPMI), and X-ray computer tomography (CT) [12, 24–26]. However, each of these techniques has its own advantages and drawbacks. The casting thin section and SEM can directly investigate the types and morphology of pore throats but fail to obtain quantitative pore-throat size distribution [27]. The HPMI can measure the size of nanoscale and microscale pore throats but might ignore the relatively large pore due to the shield effect of small pore throats [12, 28, 29]. The CPMI can distinguish pores and throats and quantitatively obtain their numbers but cannot measure the pore throats with a radius smaller than 0.12 μm because the maximum mercury intrusion pressure is 6.2 MPa [12, 30]. CT scanning is nondestructive and can reconstruct the three-dimensional image of the pore network, but its widespread application is restricted by high cost and limited resolution [31–33]. Due to the complexity of pore structure, the separate method cannot comprehensively investigate the full-scaled pore-throat size distribution of tight sandstone reservoirs [12, 34]. Therefore, the combination of various techniques to characterize the pore-throat size of tight sandstone reservoirs is necessary.

Additionally, permeability estimation has always been a concern in reservoir evaluation. Some attributes extracted from mercury injection capillary curves were frequently used to estimate permeability [35–37]. The most commonly used model is Winland model, which developed an empirical relationship between permeability, porosity, and pore-throat size corresponding to 35% mercury saturation (r_{35}) for conventional sandstone reservoirs [37]. This

model was then extended by many scholars, and lots of equations for permeability estimation were established [22, 28, 38]. Although Rezaee [22] developed an equation based on the pore-throat size corresponding to 10% mercury saturation (r_{10}) for tight sandstones, some researchers demonstrated that r_{30} was the best permeability estimator for tight sandstone reservoirs [12, 34]. The permeability estimation for tight sandstone reservoirs still remained poorly understood and controversial.

In this study, integrated methods of casting thin section, SEM, HPMI, and CPMI were conducted to study the pore structure characteristics of the Shanxi tight sandstone reservoirs in the northern Ordos Basin (China). The objectives of this paper are: (1) to investigate the full-scaled pore-throat size distribution of tight sandstone reservoirs; (2) to evaluate the effect of pore-throat size distribution on porosity and permeability; and (3) to establish a new permeability estimation model for tight sandstone reservoirs.

2. Geological Settings

The Ordos Basin is a typical intraplate craton basin located in the western part of the North China Platform [39]. As the second largest petroliferous basin in China, the Ordos Basin is tectonically stable, and its strata are evenly distributed with very low dip angles [40, 41]. The basin can be subdivided into six primary tectonic units, namely the Yimeng uplift, the Western fold-thrust belt, the Tianhuan depression, the Shanbei slope, the Jinxi flexural-fold belt, and the Weibei uplift [42]. Several tight gas fields have been discovered in the Upper Paleozoic succession of the northern Ordos Basin [43–45] (Figure 1(a)). The Hangjinqi area lies in the Yimeng uplift in the northern Ordos Basin, which has been regarded as a potential area for tight gas exploration in recent years [46–49] (Figure 1(a)). The Upper Paleozoic strata in the Hangjinqi area are composed of the Upper Carboniferous Taiyuan Formation, Lower Permian Shanxi Formation, and Middle Permian Lower and Upper Shihezi formations from bottom to top (Figure 1(b)). From the Taiyuan to Upper Shihezi Formation, the depositional environment gradually evolved from the paralic facies to the fluvial-dominated continental facies [50]. The Shanxi and Lower Shihezi Formation, which recorded deltaic and fluvial deposits, are dominated by sandy conglomerates, pebbly coarse-, coarse-, medium-, and fine-grained tight sandstones [48]. The natural gas is mainly stored in these tight sandstones with low petrophysical properties [48, 49].

3. Data and Methods

Thirty regular core cylinders (2.5 cm in diameter and 5 cm in length) were collected from the Shanxi Formation in drilling wells, and 340 porosity and permeability values were obtained from the Exploration and Development Research Institute of North China Company, Sinopec. Before all the tests, each core plug sample was washed and saturated in NaCl solution for about 24 hours to avoid clay swelling and then dried
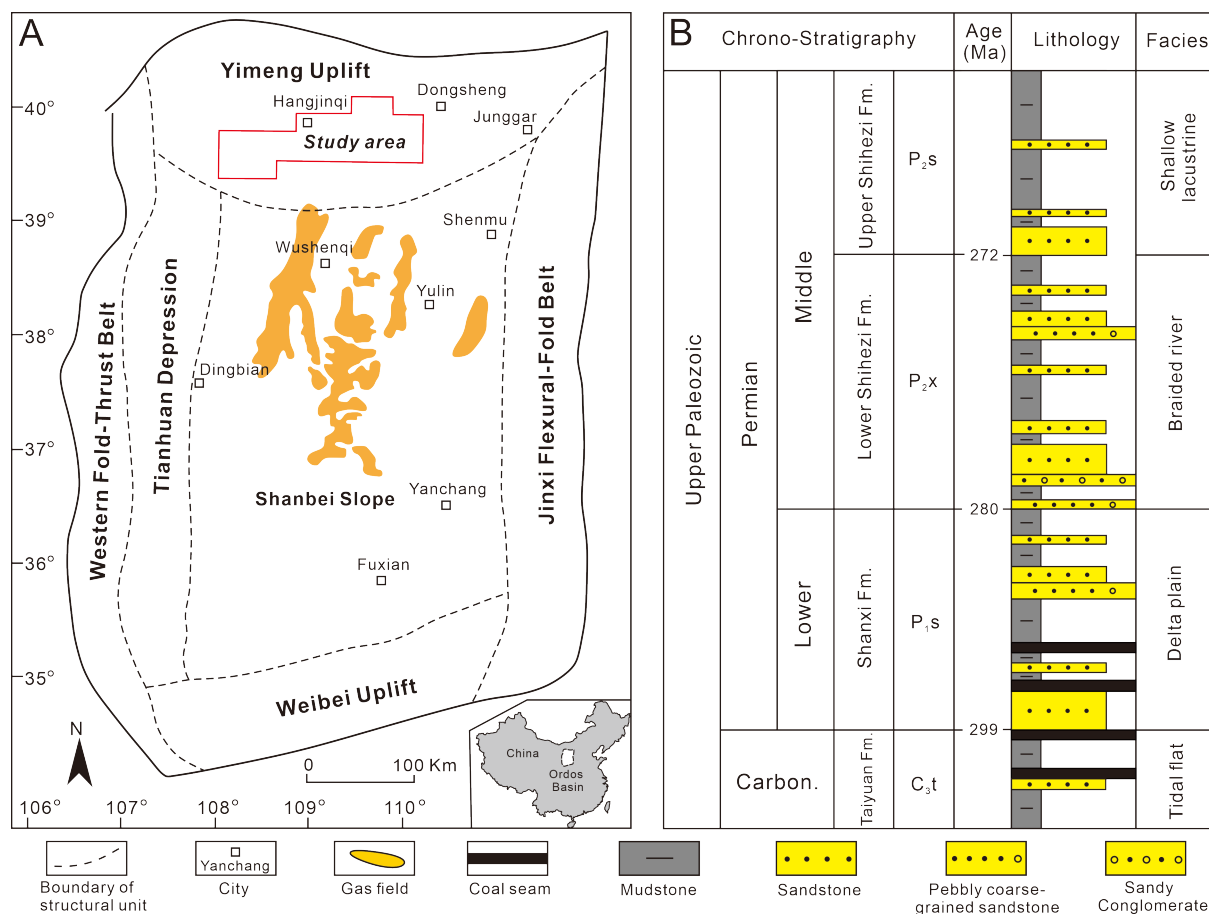
FIGURE 1: Geological map, study area (a) and stratigraphy of the Upper Paleozoic successions (b) in the north Ordos Basin (modified from Wang et al.[48] and Yang et al. [50]).

at 110°C for 24 hours under vacuum. Helium porosity and nitrogen permeability tests were first performed and then casting thin section, SEM, HPMI, and CPMI were carried out.

Casting thin sections were prepared under vacuum by impregnating with blue epoxy to highlight pores. The pore types and pore-filling minerals were observed under a Leica SKU (Stock Keeping Unit) DMLP polarizing microscope. The sandstone detrital mineral composition and grain size were determined by point counts of 350 points on each casting thin section. A Quanta 450 Field Emission Gun (FEG) SEM was used to investigate the geometry and size of different types of pores. The thin section was initially polished by (argon) Ar-ion and then coated with carbon to avoid electrostatic charges. The resolution can reach 1.2 nm with an accelerating voltage of 30 kV under a high vacuum. The average resolution applied for the samples in this study is the micrometer scale.

Six regular core cylinders were divided into two parts for HPMI and CPMI experiment, respectively. The HPMI experiment was conducted using an AutoPore IV9520 mercury porosimeter. The maximum intrusion pressure was 116 MPa, which corresponded to a pore-throat size of 0.006 μm. After reaching the highest pressure, the pressure was then gradually decreased when the mer-

cury was extruded from the samples. Both intrusion and extrusion curves were obtained. Based on the bundle of capillary tubes mode, the equivalent pore-throat radius was calculated according to the Washburn equation [51]:

$$P_c = \frac{2\sigma \cos \theta}{r}, \qquad (1)$$

where P_c (MPa) is the capillary pressure, θ (°) is the contact angle, σ (N/m) is the surface tension, and r (m) is the pore-throat radius.

The HPMI experiment was carried out using an ASPE-730 mercury porosimeter at the temperature of 25°C. The mercury was injected at a quasistatic constant rate of 0.00005 mL/min. The maximum intrusion pressure was 6.2 MPa, corresponding to a pore-throat size of 0.12 μm. The pore body and throat could be differentiated by the pressure fluctuations during mercury injection, and the total injection curve could be subdivided into the pore body injection curve and the throat injection curve. The pore body radius was calculated as a radius of equivalent spheres based on the change in the mercury volume, while the throat radius was determined by the Washburn equation. In this way, the pore body size distributions, throat size

distributions, and the pore-throat radius ratios of the six samples could be quantitatively obtained.

4. Results

4.1. Petrography and Petrophysical Properties. Point counting of thin sections shows that the Shanxi Formation sandstones are mainly sublitharenite and litharenite (Figure 2). Quartz is the most abundant mineral with an average content of 70.09%, while feldspar is rare with an average content of 0.68%. The feldspar consists of K-feldspar (average of 0.61%) and plagioclase (average of 0.07%). The rock fragments constitute an important part of the detrital minerals with an average content of 28.59%, including volcanic (average of 2.36%), metamorphic (average of 23.64%), and sedimentary rock fragments (average of 2.59%). Based on thin sections, the cements mainly include authigenic clay minerals, carbonates, and quartz overgrowths. The Shanxi Formation sandstones have a moderate textural maturity, characterized by moderate sorting and subangular to subrounded roundness. Their grain size mainly ranges from medium- (0.25 and 0.5 mm) to coarse-grained (0.5 and 2 mm). The grain contacts are mostly point-linear contacts.

Measurements from 340 tight sandstone samples show that the porosity has a wide range from 0.2% to 13.9% with an average of 6.44%, while the permeability varies between 0.037 and 14.6 mD with an average of 0.57 mD. A poor correlation between porosity and permeability is displayed (Figure 3), reflecting complex pore structure and strong heterogeneity of the Shanxi Formation tight sandstone reservoirs.

4.2. Pore and Throat Types. The pore types of Shanxi Formation tight sandstones mainly consist of intergranular pores, dissolution pores, intercrystalline micropores, and microfractures, with the relative proportion of 48.1%, 8.5%, 43%, and 0.4%, respectively. The intergranular pores have been subjected to varying degrees of modification by mechanical compaction and cementation during diagenesis. Intergranular pores occupy the spaces between grains with relatively regular shape, and their size mainly varies between 30 and 400 μm with good connectivity (Figures 4 and 5(a)–5(c)). Dissolution pores are mainly presented within partially dissolved rock fragments and feldspar grains with irregular geometry and poor connectivity (Figures 4(b)–4(e), 5(e), and 5(f)). The size of the dissolution pores is mainly in the range of 5–50 μm. However, the dissolution pores can reach more than 100 μm in radius when the feldspar grains are completely dissolved (Figure 4(e)). The intercrystalline micropores are dominant and extensively developed within the authigenic clay minerals, such as kaolinite and mixed-layer illite/smectite (Figures 4(f), 5(f), and 5(g)). Their size is commonly smaller than 10 μm with very poor connectivity. The microfractures generally occur within or cut across the brittle detrital grains and extend for tens or even hundreds of microns in length (Figures 4(a), 4(d), and 4(e)).

The throats in the Shanxi Formation tight sandstones are typically narrow because of strong mechanical compaction. The throats are dominated by sheet-like and tube-shaped throats. The sheet-like throats commonly occur where the detrital grains are in linear contacts and concave-convex contacts, which connect the intergranular pores (Figures 4(a) and 4(d)). The tube-shaped throats are mainly present within the matrix and authigenic clay minerals, which connect the micropores. Some pores and throats are connected (Figures 4(a), 4(d), and 5(h)), while the others are blocked by authigenic clay minerals, such as booklet kaolinite and filamentous illite (Figures 5(b) and 5(c)).

4.3. Pore-Throat Size Distribution

4.3.1. High-Pressure Mercury Intrusion. The HPMI-derived capillary pressure curves of the six samples are shown in Figure 6, and detailed characteristic parameters are listed in Table 2. The samples can be classified into three types according to the characteristics of intrusion curves. Type I, including samples J151-2 and J151-3, exhibits a relatively lower threshold pressure (Pd) of less than 0.4 MPa. A flat segment is displayed in the injection curves when the intrusion pressures are less than 1 MPa. The intrusion curves of Type II samples (J150-2 and J151-1) have no noticeable flat segment, and the pressures increase gradually from beginning to end (Figure 6(a)). The intrusion curves of Type III samples (J150-1 and J150-3) are steep and have no flat segment. The Type III samples have a higher medium saturation pressure of more than 30 MPa (Table 1), suggesting a bad pore structure. The maximum mercury intrusion saturations (S_m) of the six samples range from 78.83% to 96.65%, while the residual mercury intrusion saturations (S_r) vary between 43.27% and 63.92% (Table 1). The differences between the S_m and S_r suggest that large quantities of mercury were bounded in the pores due to a large pore-throat discrepancy.

Pore-throat size distributions of the samples can be obtained from the HPMI intrusion curves and Washburn equation. The six samples have a wide pore-throat size distribution with pore-throat radii ranging from 0.006 to 10 μm (Figure 6(b)). The pore-throat sizes of Type I samples show bimodal distributions, ranging from 0.006 to 2.5 μm. The pore-throat radius of the first peak is in the range of 0.006–0.1 μm with a peak value of 0.01 μm, while the second peak is between 0.1 and 2.5 μm with a peak value of 0.63 μm. The pore-throat sizes of Type II samples are characterized by unimodal distributions, varying between 0.006 and 1.6 μm with a peak value of 0.1 μm. Pore throats with radius more than 1 μm are rare in Type I and Type II samples. The Type III samples have the greatest permeabilities and largest pore-throat systems, and their pore-throat size ranges from 0.006 to 10 μm with a peak value of 1 μm. Overall, there are almost no pore throats larger than 10 μm in all the samples (Figure 6(b)), which is inconsistent with the casting thin section and SEM results. Therefore, the HPMI experiment failed to measure the relatively large pore throats.
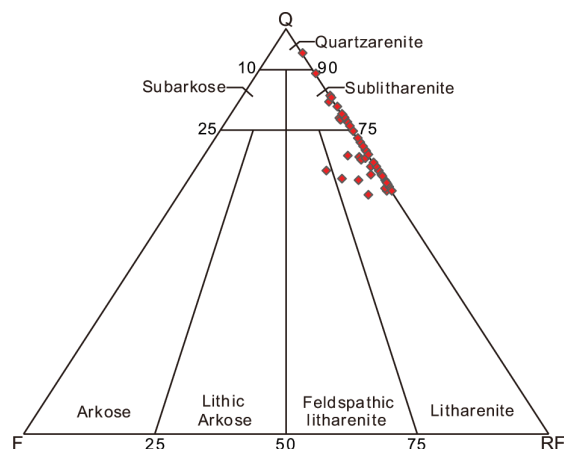
FIGURE 2: Ternary diagram illustrating the framework compositions of the Shanxi Formation sandstones (based on Folk [52]). Q: quartz; F: feldspar; RF: rock fragments.
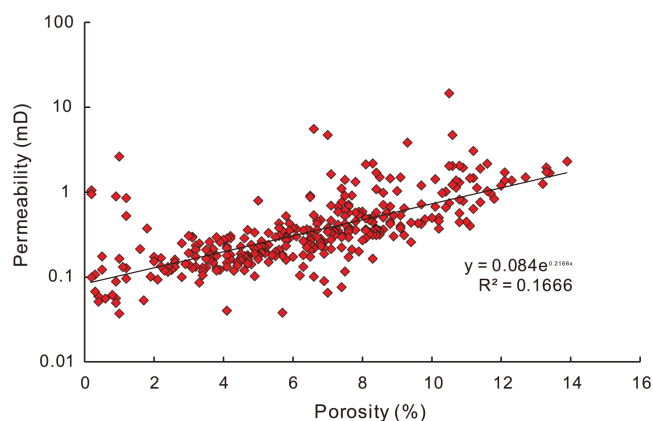

FIGURE 3: Cross-plots showing the relationship between porosity and permeability of Shanxi Formation tight sandstone reservoirs.

4.3.2. Constant-Pressure Mercury Intrusion. Unlike HPMI, the CPMI-derived capillary pressure curve can characterize pores and throats separately. The capillary pressure curves of the six samples show similar characteristics (Figure 7). The trend of the total mercury injection curve is in accordance with the throat mercury injection curve at the initial stage. As the entry pressures increase, the mercury saturation of the pore bodies rapidly increases over a narrow range of capillary pressures, while the mercury saturation of the throats continuously increases to the end (Figure 7). The maximum mercury injection saturation of the throats ranges from 37.24% to 56.62% with an average of 46.81%, while the maximum mercury injection saturation of the pore bodies varies between 2.69% and 22.03% with an average of 12.55% (Table 1). The mercury injection saturation of the pore bodies is much lower than that of the throats, suggesting that most of the pore throats in the tight reservoirs are unconnected. In addition, the total mercury injection saturations of these six samples (average of 59.36%) are highly different from that of HPMI experiments (average of 84.77%). This is because the maximum

applied injection pressure of the CPMI experiments is 6.2 MPa, which is much lower than that of the HPMI experiments (200 MPa). Therefore, the mercury cannot enter the tiny pore in the CPMI experiment, resulting in some loss in pore volume.

The pore body size of these six samples exhibits a similar distribution pattern and minor variation (Figure 8(a)). The pore body radius ranges from 100 to 525 μm, and the main distribution interval is 100–200 μm. The average pore body radius was between 150 and 171.56 μm with an average of 160.51 μm. The pore radius displays a positive correlation with porosity ($R^2 = 0.5583$) and permeability ($R^2 = 0.6019$). The throat radius ranges from 0.5 to 11.5 μm, and the main distribution interval is between 0.5 and 4 μm. It is worth noting that the throat size varies greatly as a function of the permeability (Figure 8(b)). The distribution range of throat size becomes wider as the permeability increases. For sample J151-3 with a high permeability ($K = 1.49$ mD), the throat radius ranges from 1 to 10 μm with an average value of 2.31 μm. However, for sample J151-1 with low permeability ($K = 0.264$ mD), the throat radius ranges from 0.5 to 1.9 μm with an average value of 0.86 μm (Figure 8(b)). The throat radius is positively correlated with porosity ($R^2 = 0.5299$) and permeability ($R^2 = 0.8063$) (Figures 9(c) and 8(d)). The better correlation between the throat radius and permeability indicates that throat size is the crucial factor controlling the permeability in the tight sandstone reservoirs. The pore-throat radius ratio (defined as the ratio of the pore body radius to the throat radius) can reflect the pore-throat connectivity. The similar pore body radius and varying throat radius lead to a wide range of pore-throat radius ratio from 10 to 400 (Figure 8(c)). The average pore-throat radius ratio ranges from 102.81 to 171.56 with an average of 160.51. The pore-throat radius ratio has no obvious correlation with porosity but a good negative correlation with permeability ($R^2 = 0.8449$) (Figures 9(e) and 9(f)). This indicates that a big pore-throat radius ratio is primarily responsible for the low permeability of a tight sandstone reservoir.

5. Discussions

5.1. Full Scale of Pore-Throat Size Distribution. Neither HPMI nor CPMI experiment can separately investigate the full-scaled pore-throat size distribution because of the various types and scales of pores in the Shanxi tight sandstone reservoirs. Although the HPMI can investigate relatively smaller pore throats under high-pressure conditions, it lost sight of relatively larger pores (mainly larger than 10 μm) due to the shielding effect of the small pore throats. Moreover, the HPMI cannot distinguish between pores and throats, and it actually records information about the throat distribution [29]. In contrast, the CPMI can reveal the distribution characteristics of both pores and throats based on the pressure fluctuations when mercury was injected at a constant rate. However, it fails to measure the pore throats with the radii smaller than 0.12 μm due to the limited injection pressure. Therefore, the
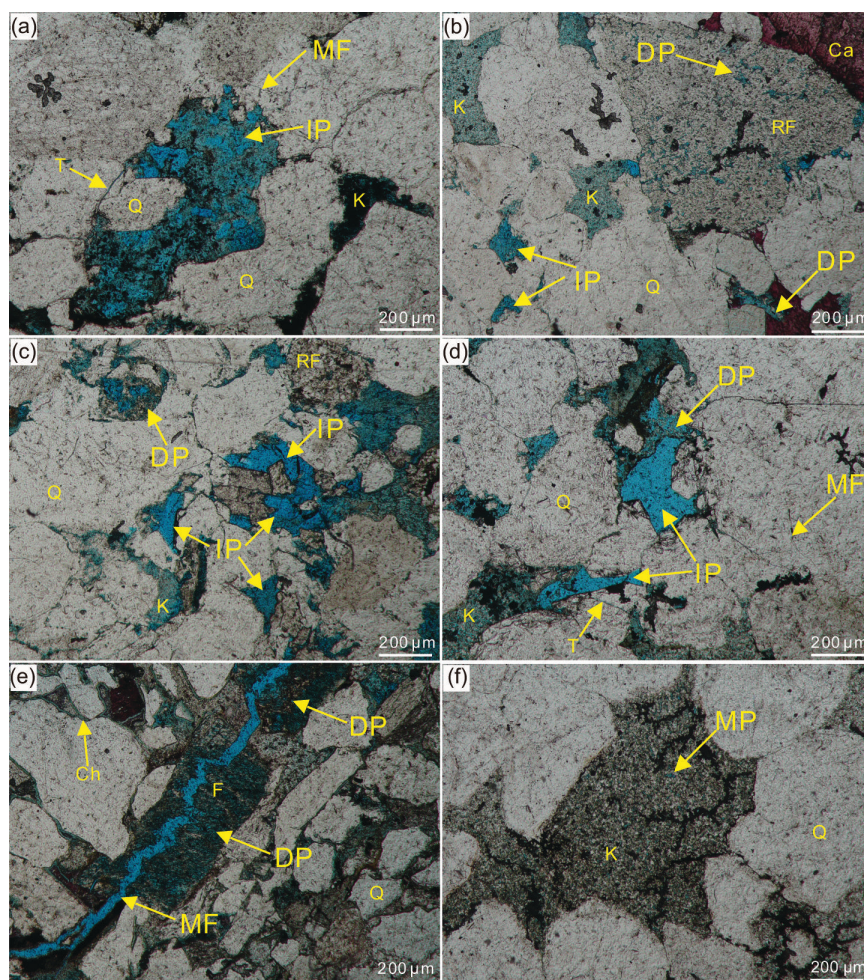
FIGURE 4: Casting thin section microphotographs showing pore types of the Shanxi Formation tight sandstone reservoirs. (a) Intergranular pore (Well J70, 2872.87 m); (b) intergranular pore and dissolution pore (Well J87, 3072.83 m); (c) intergranular pore and dissolution pore (Well J93, 3060.93 m); (d) intergranular pore and dissolution pore (Well J73, 3138.89 m); (e) dissolution pore and microfracture (Well J82, 2626.1 m); and (f) intercrystalline micropores (Well J72, 3013.47 m). IP: intergranular pores; DP: dissolution pore; MP: micropore; MF: microfracture; T: throat; Q: quartz; F: feldspar; K: kaolinite; RF: rock fragment; Ca: calcite; Ch: chlorite.

full scale of pore-throat size distribution of tight sandstone reservoirs was obtained by combining the HPMI and CPMI in this study.

Because of the same physical procedure reflected by the HPMI and CPMI experiments, the mercury intrusion curves obtained by the two methods should be consistent [12]. However, taking sample J151-3 for instance, the intrusion curves of HPMI and CPMI display some discrepancy. The total mercury injection saturation of CPMI is always higher than that of HPMI at the same capillary pressure (Figure 10(a)). Such difference might be caused by the following three reasons: (1) A quasistatic velocity is kept when the mercury is injected, and therefore, the interfacial tension and contact angle remain unchanged during the CPMI experiment. However, the high injection velocity of the HPMI experiment would produce a wetting hysteresis effect, making contact angle change and causing an inconsistency [12,51]. (2) Some pores like slit-shaped pores may act as both pores and throats [29]. For these pores, the results obtained by HPMI and CPMI experi-

ments should be theoretically similar. However, the Shanxi sandstone reservoirs actually have complex pore structure and diverse pore morphology. Therefore, the discrepancies might be created when the pore geometries are deviated from slit-shaped pores [34]. (3) The targets for the HPMI and CPMI experiments came from the same core plug sample. Therefore, the results might be different due to the strong heterogeneity of pore structure in tight sandstones [53]. Additionally, some researchers proposed that high injection pressure during the HPMI experiment would result in the compression of grains, which may cause the capillary curve to shift [9, 12]. However, the Shanxi sandstones are rich in quartz (Figure 2), meaning that the tested samples are strong to compression, and therefore, the capillary curves are less likely to be shifted in the HPMI experiment [34].

Although there are some differences between the HPMI and CPMI experiments, the combination of the two techniques is still an effective method to characterize the full scale of pore-throat size distribution of tight sandstone
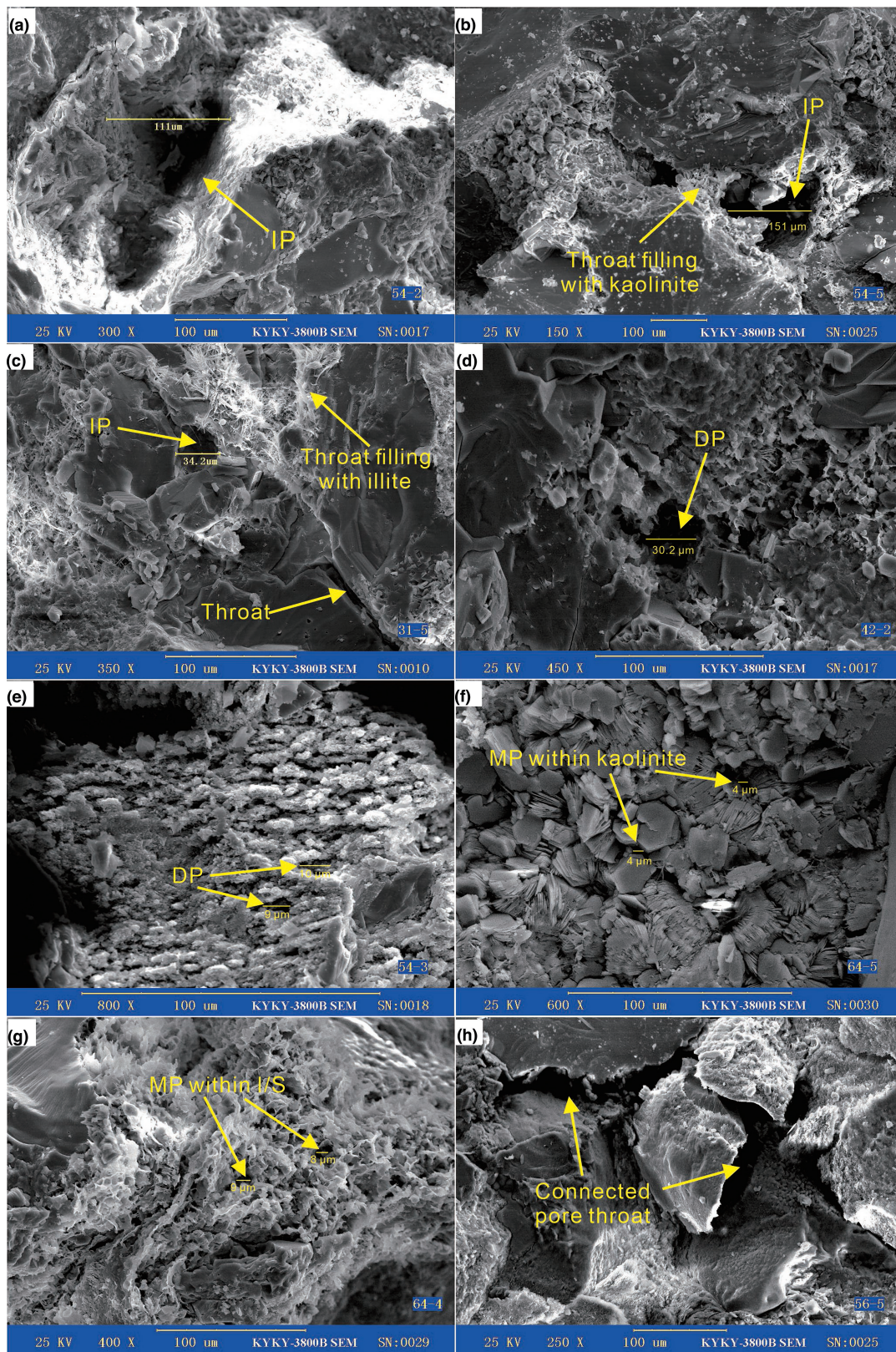
FIGURE 5: SEM photographs showing pore types and sizes of Shanxi Formation tight sandstone reservoirs. (a) Intergranular pore (Well J75, 2803.5 m); (b) intergranular pore (Well J89, 3164.48 m); (c) intergranular pore (Well J76, 2730.26 m); (d) dissolution pore (Well J89, 3163.08 m); (e) dissolution pore (Well J75, 2803.5 m); (f) intercrystalline micropores (Well J89, 3173.15 m); (g) intercrystalline micropores (Well J89, 3173.15 m); (h) connected pore throat (Well J92, 3073.88 m). IP: intergranular pores; DP: dissolution pore; MP: micropore; I/S: mixed-layer illite/smectite.
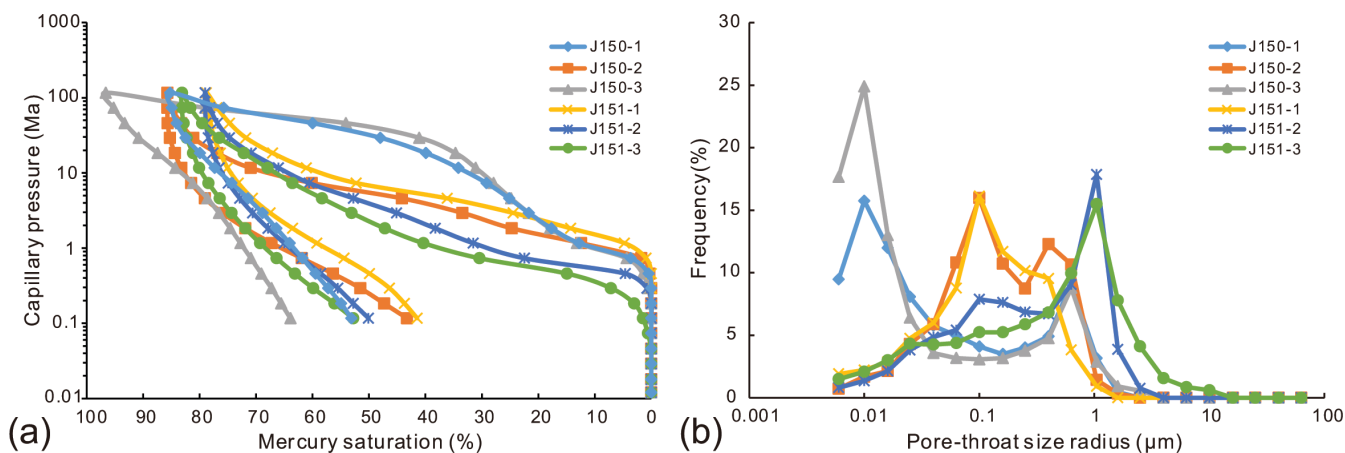
FIGURE 6: HPMI-derived mercury injection and extrusion curves (a) and the distributions of pore-throat size (b).

TABLE 1: Pore structure characteristic parameters of the Shanxi Formation sandstone samples.

| Samples | Depth (m) | ϕ (%) | K (mD) | HPMI | | | | CPMI | | | |
				P_t (MPa)	P_{50} (MPa)	S_m (%)	S_r (%)	P_t (MPa)	S_f (%)	S_b (%)	S_t (%)
J150-1	3536.8	4.7	0.358	0.56	31.28	85.23	53.14	0.36	45.79	8.55	37.24
J150-2	3537.95	9.2	0.312	0.66	5.32	85.71	43.27	0.4	66.63	10.01	56.62
J150-3	3542.45	4.2	0.304	0.52	39.02	96.65	63.92	0.38	49.69	12.74	36.95
J151-1	3567.65	5.1	0.264	0.83	6.77	78.83	41.49	0.78	54.88	2.69	52.19
J151-2	3577.34	11.7	0.966	0.39	3.82	79.04	50.1	0.34	69.8	19.3	50.5
J151-3	3579.32	9.1	1.49	0.19	2.24	83.14	52.81	0.28	69.4	22.03	47.37

K and ϕ represent the permeability and porosity, respectively. P_t, P_{50}, S_m, and S_r represent the threshold pressure, medium saturation pressure, maximum mercury intrusion saturation, and residual mercury saturation of HPMI, respectively. S_f, S_b, and S_t represent the final mercury intrusion saturation, pore body mercury saturation, and pore-throat saturation of CPMI, respectively.

TABLE 2: Controls of the nanopores on the pore volume and permeability of tight sandstone reservoirs.

Sample	Depth (m)	Φ (%)	K (mD)	Pore volume controlled by nanopores (%)	Permeability contribution controlled by nanopores (%)
J150-1	3536.8	4.7	0.358	72.47	9.98
J150-2	3537.95	9.2	0.312	73.27	17.93
J150-3	3542.45	4.2	0.304	83.49	22.87
J151-1	3567.65	5.1	0.264	74.07	50.41
J151-2	3577.34	11.7	0.966	47.49	2.94
J151-3	3579.32	9.1	1.49	42.76	0.76

reservoirs. By merging the pore size distribution curves of the two methods at where they overlapped, the overall pore size distribution curves of the Shanxi tight sandstone reservoirs were obtained. The curves display multimodal with pore sizes ranging from 0.006 to 525 μm in radii (Figure 10(b)). Each curve has two main peaks, which correspond to the throats and pore bodies, respectively. The right peak covers 100–525 μm with a peak value of approximately ~135 μm, which represents the distribution characteristic of pore bodies and shows no obvious difference among samples (Figure 10(b)). Pores in this size range are mainly associated with intergranular pores, which were mainly formed as a result of varying degrees of compaction and cementation in the Permian tight sandstones in the north Ordos Basin. Compaction resulted in a reduction of more than half of the original porosity, while calcite and quartz cements accentuate the variations in the size of the intergranular pore [19, 55]. The left peak spans 0.006–15 μm, which reflects the distribution characteristic of throats and displays significant variation between different samples (Figure 10(b)). The pores in this range are related to intercrystalline micropores, dissolution pores, and microfractures. The fluctuations of curves in this pore range are probably caused by the high clay mineral content and
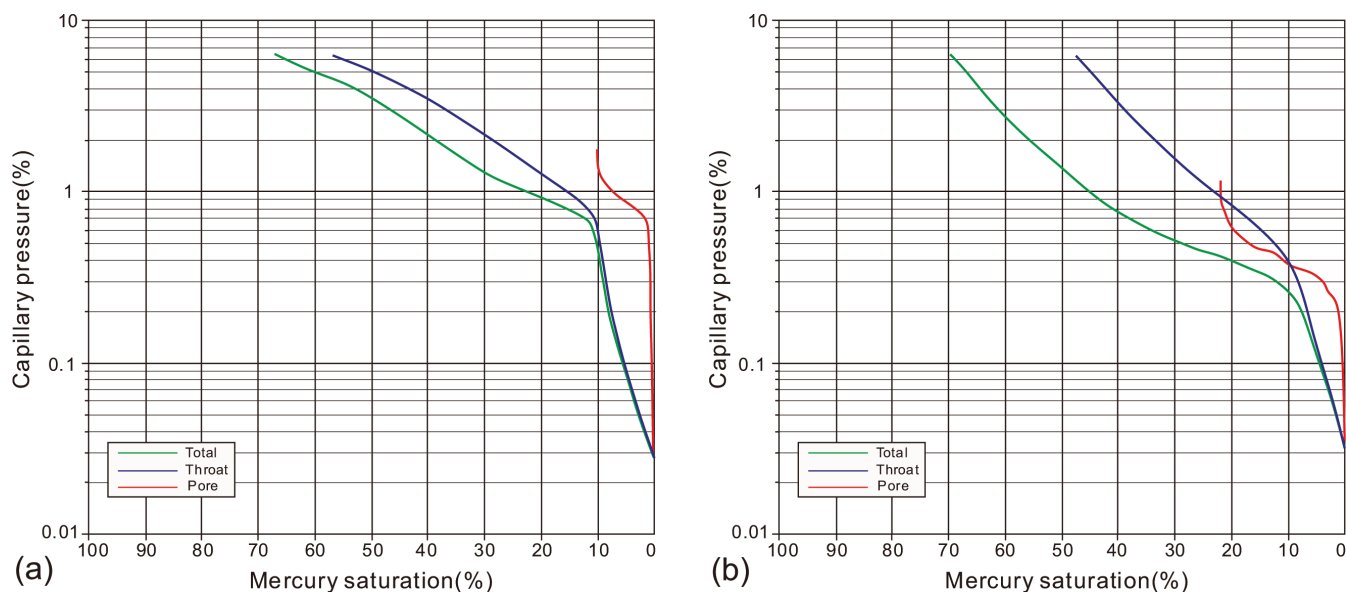
FIGURE 7: The total mercury injection curves, pores mercury injection curves, and throats mercury injection curves obtained from CPMI. (a) J150-2 and (b) J151-3.
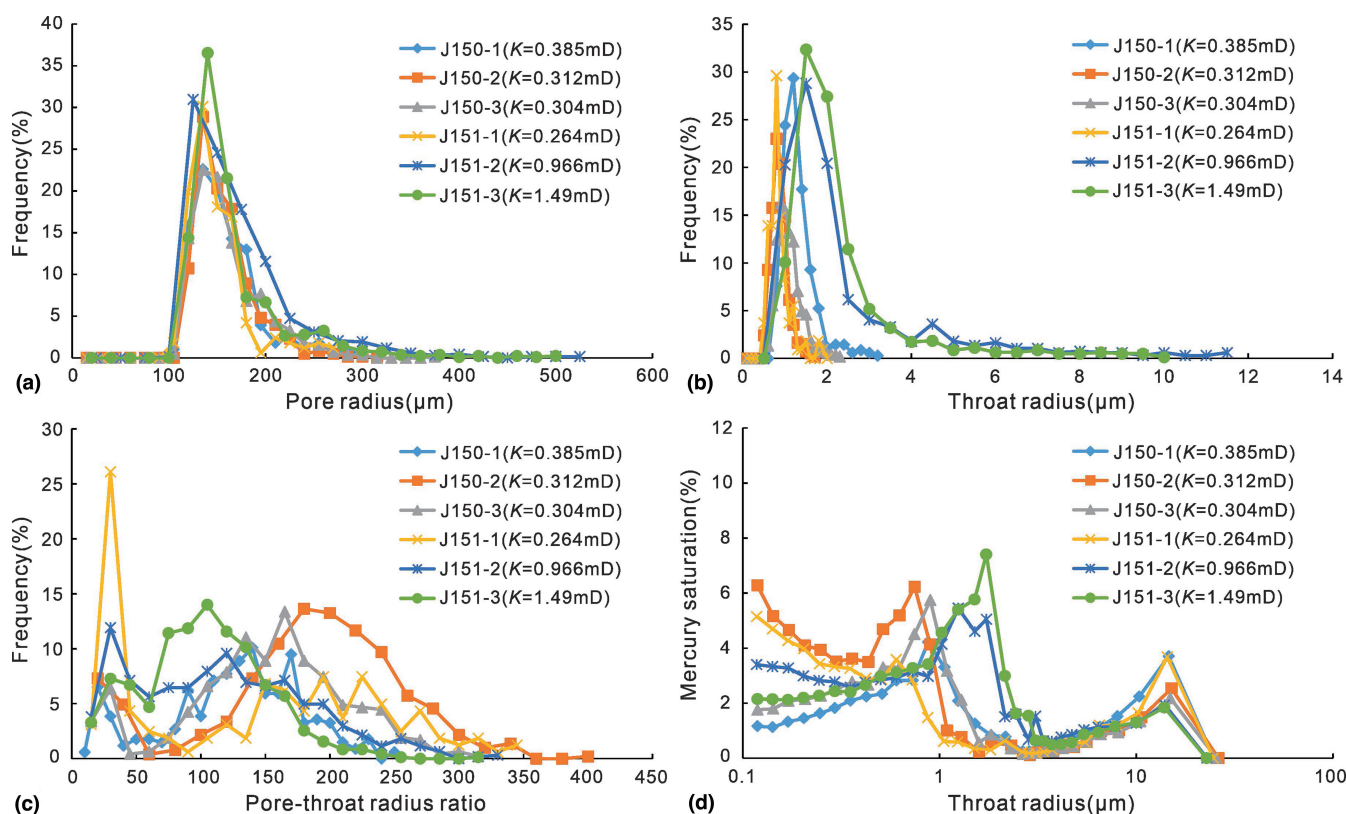

FIGURE 8: Distribution characteristics of pore-throat parameters obtained from CPMI. (a) The distributions of pore radius, (b) the distributions of throat radius, (c) the distributions of pore-throat radius ratio, and (d) the relationships between the mercury injection saturation and the throat radius.

various pore types in the tight reservoirs [12]. Clay mineral type, content, occurrence, and distribution in different lithofacies of the Permian tight sandstones have variable effects on pore-throat size distribution [19, 48]. Clay minerals generally fill the intergranular and dissolution

pores and block the connected pores and throats, causing a smaller pore throat radius and poor connectivity. Meanwhile, substantial microscopic pores within the clay minerals further complicated the pore network [54]. The pores with radii smaller than 3 μm are dominant and
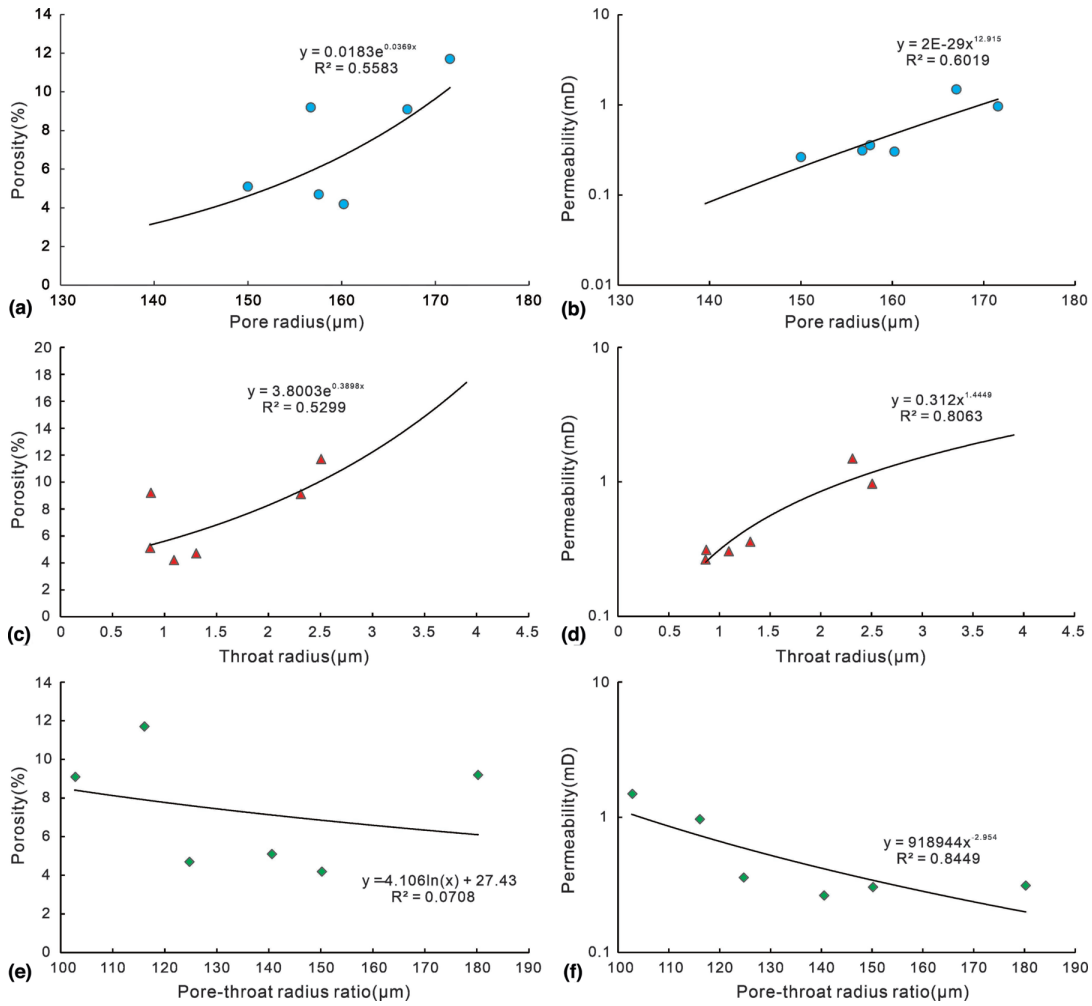
FIGURE 9: Cross-plots showing relationships between porosity and permeability and pore radius (a and b), throat radius (c and d), and pore-throat radius ratios (e and f) obtained from CPMI.
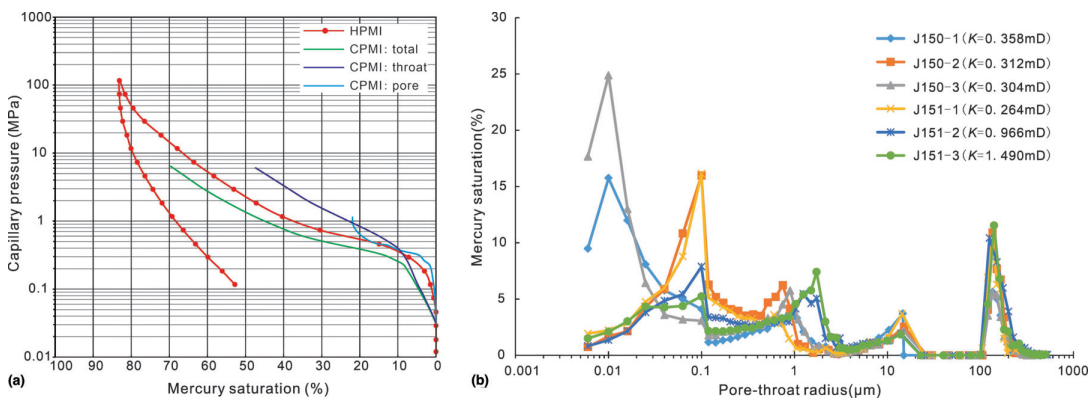

FIGURE 10: Comparison of mercury injection curves of HPMI and CPMI (J151-3) (a) and full range of pore-throat size distribution curves (b).

exhibit multiple peaks, while the pores with radii between 3 and 15 μm are few, and pores in the range of 15–100 μm almost do not occur (Figure 10(b)). According to the classification scheme proposed by Loucks et al. [55], the pores are divided into macropores (>2 mm), mesopores (30–2 mm), micropores (0.5 and 30 μm), and nanopores

(<0.5 μm). The pore size distribution curves show that Shanxi Formation sandstone reservoirs mainly consist of nanopores, micropores, and mesopores.

It is worth noting that the porosity of samples J150-2 and J151-3 is exactly similar (9.2% and 9.1%, respectively), but the permeability is highly different

(0.312% and 1.64%, respectively) (Table 1). Such difference is probably attributed to similar pore body size but different throat size distribution between the two samples (Figure 10(b)). The throat size of sample J150-2 mainly ranges from 0.006 to 2.8 μm with a peak value of ~0.1 μm while that of sample J151-3 mainly varies between 0.006 and 3.7 μm with a peak value of ~1.7 μm, resulting in a lower pore-throat radius ratio of sample J151-3 than that of sample J151-3. It is indicated that pore-throat size distribution, especially the throat size, plays an important role in the petrophysical properties of tight sandstone reservoirs.

5.2. Pore-Throat Size Controls on Petrophysical Properties of Reservoir. The cumulative mercury injection saturation curve and cumulative permeability contribution curve directly obtained from the HPMI experiment can be used to characterize the reservoir storage capacity and percolation potential, respectively. The cumulative permeability contribution rapidly increases to the near maximum during the early stage of mercury injection and then remains essentially unchanged after that (Figure 11), indicating that the permeability is primarily controlled by a small amount of relatively large pore throats. However, the cumulative mercury injection saturation continues to increase throughout the whole injection process (Figure 11), suggesting that the porosity is affected by the various scales of pore throats. For the four samples, when the cumulative permeability contributions increase to 98%, 97%, 99%, and 98%, respectively, the cumulative mercury saturations are just 30.43%, 31.05%, 44.18%, and 36.17%, respectively, suggesting that the mercury saturations of 69.57%, 68.95%, 55.82%, and 63.83% are controlled by the relatively smaller pore throats (Figure 11). This indicates that the relatively smaller pore throats with a large percentage contribute little to the permeability but significantly improve the storage capacity of the tight sandstone reservoirs. Additionally, the peak of the permeability contribution curve moves to the left as the permeability decreases (Figure 11). The peak value displays a strong positive correlation with the permeability (Figure 12(a)), indicating that the proportion of smaller pore throats increases as the permeability decreases.

Nanopores, as a dominant pore type in the Shanxi tight sandstone reservoir, contribute little to the permeability (Figure 11). To quantitatively investigate the effect of nanopores on the petrophysical properties of reservoirs, the HPMI curves are analyzed, and the cumulative mercury injection saturations and cumulative permeability contributions from pore throats with a radius smaller than 0.5 μm are calculated for all samples. For the samples with permeability less than 0.9 mD, the contributions from pore throats with a radius smaller than 0.5 μm to pore volume range from 72.47% to 83.49% with an average of 75.83%, while the contributions to permeability vary between 9.98% and 50.41% with an average of 25.3% (Table 2). This suggests that

nanopores play a significant role in the storage capacity of reservoirs. However, for the samples with permeability greater than 0.9 mD, the contributions from pore throats with a radius smaller than 0.5 μm to pore volume and permeability were in the range of 42.76%–47.49% (an average of 45.13%) and 0.76%–2.94% (an average of 1.85%), respectively (Table 2). In this case, the impact of nanopores on the percolation potential of reservoirs is negligible. Therefore, it is inferred that the higher the permeability, the smaller the proportion of pore volumes controlled by nanopores, and the smaller the permeability contribution (Figure 12(b)).

5.3. New Permeability Estimation Model. It is accepted that the permeability is mainly controlled by the pore throats that are larger than the medium pore-throat radius (r_{50}) in the tight sandstone reservoirs [20, 54]. Several models have been developed to predict the permeability of sandstone reservoirs using pore-throat radius from mercury injection capillary pressure [20, 26, 37]. The common models such as those of the Winland [37], Pittman [26], and Rezaee [20] are, respectively, as follows:

$$\log r_{35} = 0.732 + 0.588 \log K_{\text{air}} - 0.864 \log \varphi, \quad (2)$$

$$\log K = -1.221 + 1.415 \log \varphi + 1.512 \log r_{25}, \quad (3)$$

$$\log K = -1.92 + 0.949 \log \varphi + 2.18 \log r_{10}, \quad (4)$$

where K is the air permeability (mD), ϕ is the porosity (%), and r_{35}, r_{25}, and r_{15} represent the pore-throat radius (μm) corresponding to 35%, 25%, and 15% mercury saturation on cumulative mercury intrusion curves, respectively.

These three models are used to calculate the estimated permeabilities of the Shanxi Formation tight sandstone reservoirs. The estimated permeabilities display a poor correlation with the measured permeabilities (Figure 13(a)), indicating that the empirical models are not suitable for the investigated tight sandstone reservoirs in the study area. To determine the optimal pore-throat radius, multiple regressions are carried out to evaluate the relationship between permeability, porosity, and pore-throat radius (r_{10}–r_{50}). The empirical equations and corresponding correlation coefficients are listed in Table 3. The r_{10}–r_{20} exhibit good correlations with the permeability, and the correlation coefficients (R^2) are greater than 0.9. The r_{15} yields the highest correlation coefficient of 0.9626, which is the best permeability estimator for tight gas reservoirs (Table 3). The corresponding empirical equation is expressed as:

$$\log K = -0.043 + 1.253 \log r_{15} - 0.137 \log \phi, \quad (5)$$

where K is the air permeability (mD), ϕ is the porosity (%), and r_{15} represents the pore-throat radius (μm) corresponding to 15% mercury saturation on cumulative mercury intrusion curves.
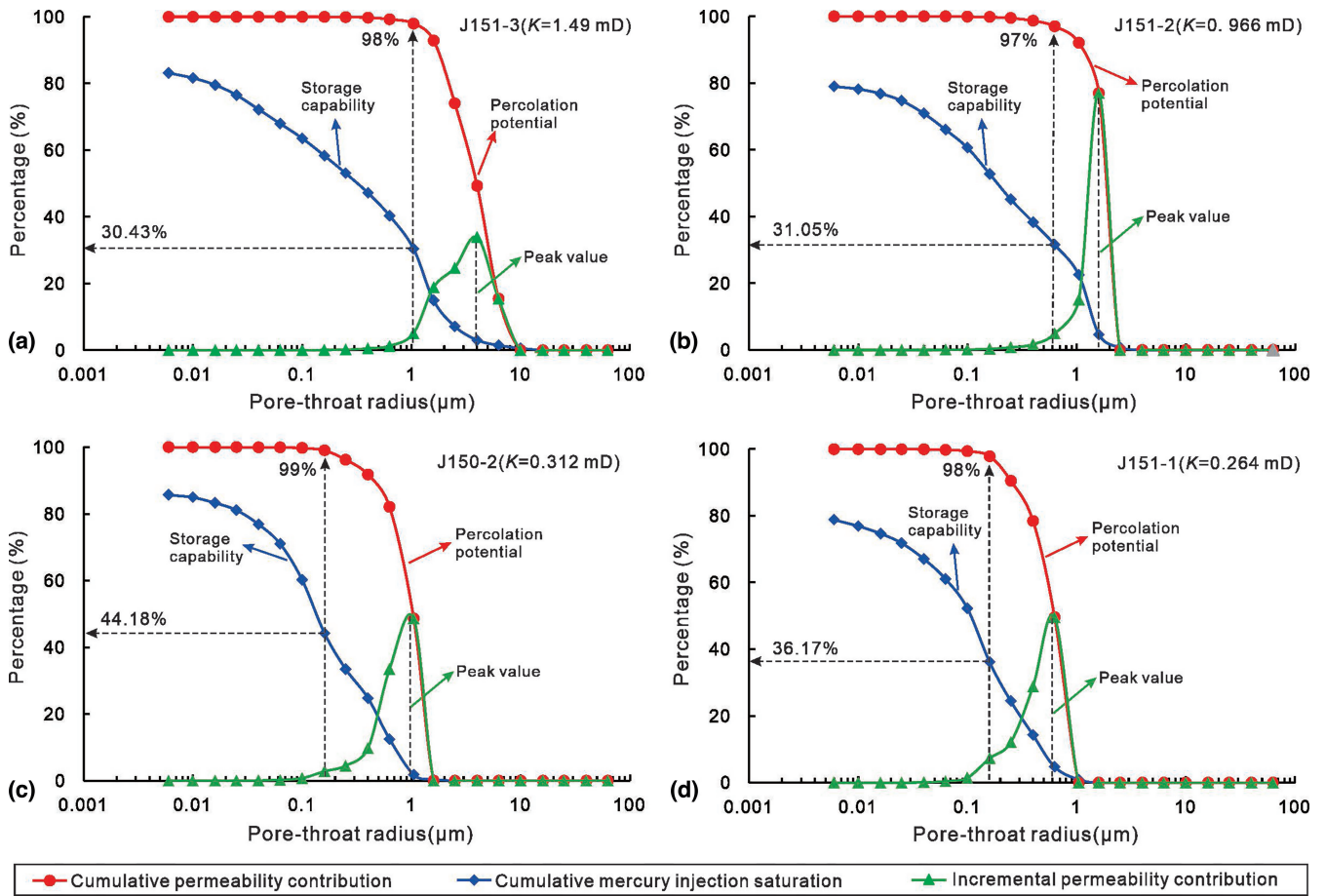
FIGURE 11: Controls of the pore-throat size on the storage capability and percolation potential of tight gas sandstone reservoirs.
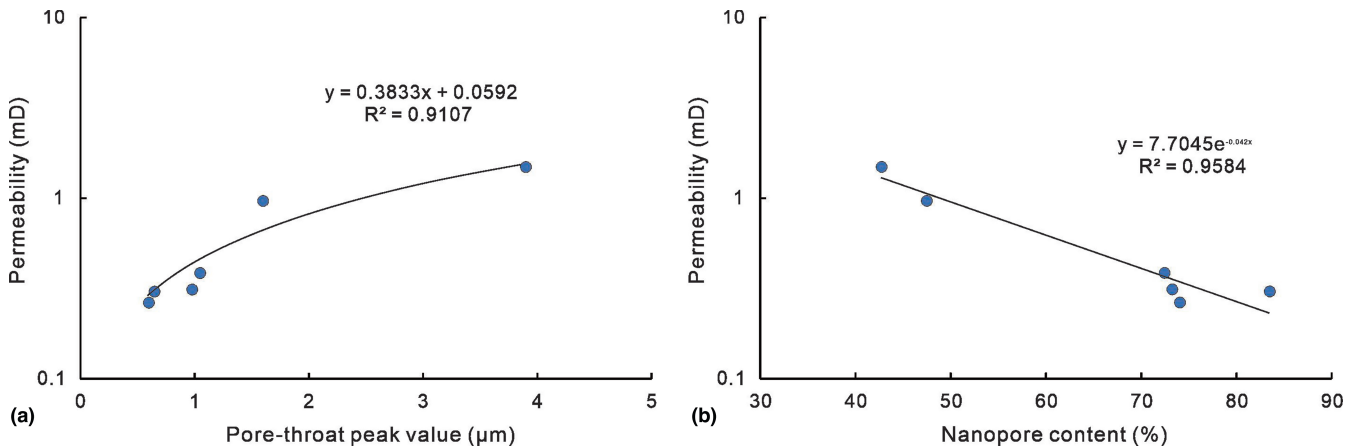

FIGURE 12: Cross-plots showing the relationship between permeability and pore-throat peak value (a) and nanopore content (b).

The measured permeabilities match well with the permeabilities estimated from the new equation with r_{15} (Figure 13(b)). The models proposed by Winland [33] and Pittman [22] are actually specific to conventional sandstones, and therefore, they are not applicable for tight sandstones because tight sandstones have a more complex pore network than that of conventional sandstones. For the investigated tight sandstones, the pore-throat radius corresponding to higher mercury saturation (e.g., 25% or 35%) falls into the range of nanopores, which contributes a little to permeability. The empirical model developed by Rezaee [22] using r_{10} is for the tight sandstones, and the permeabilities estimated by this model display a relatively better correlation with the measured permeabilities than that of the other two models. This indicates that the pore-throat radius corresponding to lower mercury saturation is a better permeability predictor for tight sandstone
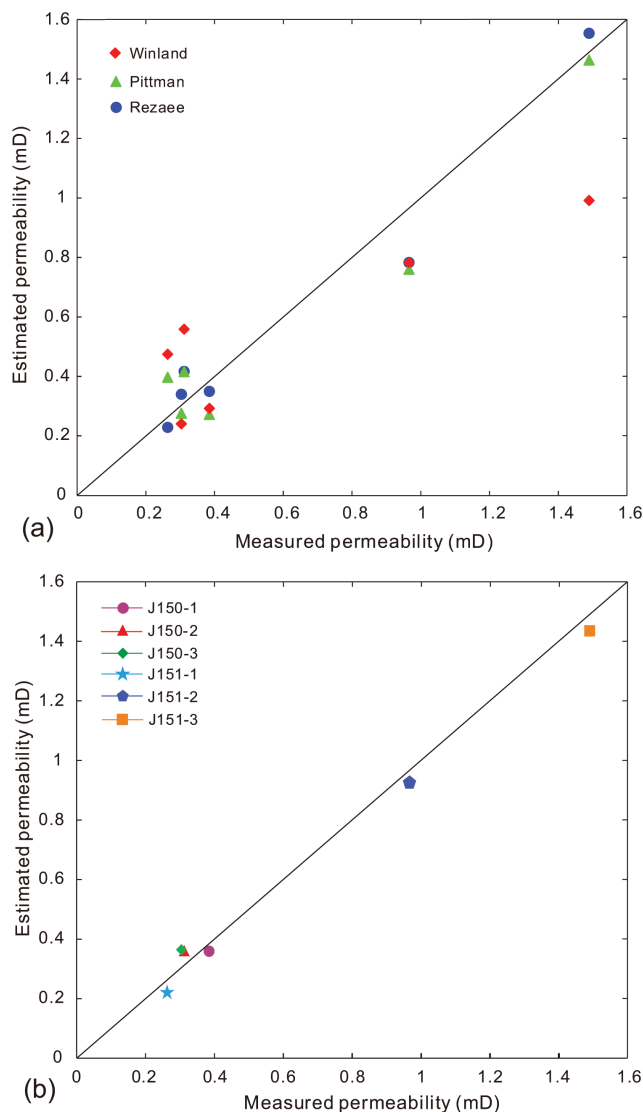
FIGURE 13: Cross-plots showing the relationship between the measured and calculated permeability: (a) calculated permeability from the Winland model (1980), Pittman model (1992), and Rezaee model (2012); (b) calculated permeability from Equation 5.

TABLE 3: Equations developed from regression analysis. R^2 is between the measured permeability and estimated permeability for different throat radii.

Equations	R^2
$\log K = -0.484 + 1.095 \log r_{10} - 0.260 \log \phi$	0.9334
$\log K = -0.043 + 1.253 \log r_{15} - 0.137 \log \phi$	0.9629
$\log K = 0.427 + 1.262 \log r_{20} - 0.454 \log \phi$	0.9096
$\log K = 0.797 + 1.083 \log r_{25} - 0.758 \log \phi$	0.8300
$\log K = 0.453 + 0.708 \log r_{30} - 0.416 \log \phi$	0.6854
$\log K = 0.015 + 0.463 \log r_{35} + 0.022 \log \phi$	0.6019
$\log K = -0.105 + 0.396 \log r_{40} + 0.172 \log \phi$	0.6046
$\log K = -0.744 + 0.170 \log r_{50} + 0.738 \log \phi$	0.4923

reservoirs. However, the r_{10} is not the best for investigated tight gas sandstones, suggesting that different tight sandstones have varying pore network complexity. The tight sandstones investigated by Rezaee [22] are mainly arkose to lithic-arkose, while the Shanxi Formation tight sandstones are mainly litharenite to sublitharenite. The different mineral composition might affect diagenesis and result in the complexity of pore structure.

6. Conclusions

The study of the pore-throat size distribution and its effect on the petrophysical properties of the Shanxi Formation tight sandstones in the northern Ordos Basin (China) allows the following conclusions:

(1) Pore types of the tight gas sandstone reservoirs in the study area include intergranular pores, dissolution pores, intercrystalline micropores, and microfracture, while the throats are dominated by sheet-like and tube-shaped throats. The HPMI-derived pore-throat size ranges from 0.006 to 10 μm, and the pore throats with radius larger than 10 μm are less frequent. The pore body size distributions obtained from CPMI show similar characteristic with radii ranging from 100 to 525 μm, while the throat size distributions vary greatly with radii ranging from 0.5 to 11.5 μm, resulting in a strong heterogeneity of pore-throat radius ratio.

(2) The full range of pore size distribution curves obtained from the combination of HPMI and CPMI displays multimodal with radii ranging from 0.006 to 525 μm. Permeability of the tight sandstone reservoirs was primarily controlled by relatively larger pore throats with small proportions, and the permeability decreases as the proportion of smaller pore throats increases. The pervading nanopores in the tight sandstone reservoirs contribute little to the permeability but play an important role in the reservoir storage capacity.

(3) A new empirical equation obtained by multiple regression indicates that r_{15} is the best permeability estimator for tight gas sandstone reservoirs, which yields the highest correlation coefficient of 0.9629 with permeability and porosity.

References

[1] J. X. Dai, Y. Y. Ni, and X. Q. Wu, "Tight gas in China and its significance in exploration and exploitation," *Petroleum Exploration and Development*, vol. 39, no. 3, pp. 277–284, 2012.

[2] C. Z. Jia, "Breakthrough and significance of unconventional oil and gas to classical petroleum geology theory," *Petroleum Exploration and Development*, vol. 44, no. 1, pp. 1–10, 2017.

[3] C. Zou, G. Zhang, Z. Yang, et al., "Concepts, characteristics, potential and technology of unconventional hydrocarbons: On unconventional petroleum geology," *Petroleum Exploration and Development*, vol. 40, no. 4, pp. 413–428, 2013.

[4] J. Dai, C. Yu, S. Huang, et al., "Geological and geochemical characteristics of large gas fields in China," *Petroleum Exploration and Development*, vol. 41, no. 1, pp. 1–13, 2014.

[5] L. D. Sun, C. N. Zou, A. L. Jia, et al, "Development characteristics and orientation of tight oil and gas in China," *Petroleum Exploration and Development*, vol. 46, pp. 1015–1026, 2019.

[6] K. Wimmers and B. Koehrer, "Integration of sedimentology, petrophysics and rock typing as key to understanding a tight gas reservoir," *Oil Gas European Magazine*, vol. 40, pp. 196–200, 2014.

[7] J. Fic and P. K. Pedersen, "Reservoir characterization of a 'tight' oil reservoir, the middle jurassic upper shaunavon member in the whitemud and eastbrook pools, SW Saskatchewan," *Marine and Petroleum Geology*, vol. 44, June, pp. 41–59, 2013.

[8] K. W. Shanley and R. M. Cluff, "The evolution of pore-scale fluid-saturation in low-permeability sandstone reservoirs," *AAPG Bulletin*, vol. 99, no. 10, pp. 1957–1990, 2015.

[9] K. Xi, Y. Cao, B. G. Haile, et al., "How does the pore-throat size control the reservoir quality and oiliness of tight sandstones? the case of the lower cretaceous quantou formation in the southern Songliao Basin, China," *Marine and Petroleum Geology*, vol. 76, September, pp. 1–15, 2016.

[10] S. B. Coskun and N. C. Wardlaw, "Image analysis for estimating ultimate oil recovery efficiency by waterflooding for two sandstone reservoirs," *Journal of Petroleum Science and Engineering*, vol. 15, nos. 2–4, pp. 237–250, 1996.

[11] J. Lai and G. Wang, "Fractal analysis of tight gas sandstones using high-pressure mercury intrusion techniques," *Journal of Natural Gas Science and Engineering*, vol. 24, May, pp. 185–196, 2015.

[12] H. Zhao, Z. Ning, Q. Wang, et al., "Petrophysical characterization of tight oil reservoirs using pressure-controlled porosimetry combined with rate-controlled porosimetry," *Fuel*, vol. 154, August, pp. 233–242, 2015.

[13] Y. Zhou, S. Wu, Z. Li, et al., "Investigation of microscopic pore structure and permeability prediction in sand-conglomerate reservoirs," *Journal of Earth Science*, vol. 32, no. 4, pp. 818–827, 2021.

[14] M. Xiao, S. Wu, X. Yuan, and Z. Xie, "Conglomerate reservoir pore evolution characteristics and favorable area prediction: A case study of the lower triassic baikouquan formation in the northwest margin of the Junggar Basin, China," *Journal of Earth Science*, vol. 32, no. 4, pp. 998–1010, 2021.

[15] S. Morad, K. Al-Ramadan, J. M. Ketzer, and L. F. De Ros, "The impact of diagenesis on the heterogeneity of sandstone reservoirs: A review of the role of depositional facies and sequence stratigraphy," *AAPG Bulletin*, vol. 94, no. 8, pp. 1267–1309, 2010.

[16] P. H. Nelson, "Pore-throat sizes in sandstones, tight sandstones, and shales," *AAPG Bulletin*, vol. 93, no. 3, pp. 329–340, 2009.

[17] K. Liu, R. Wang, W. Shi, et al, "Diagenetic controls on reservoir quality and heterogeneity of the triassic chang 8 tight sandstones in the binchang area (Ordos Basin, China)," *Marine and Petroleum Geology*, vol. 146, December, p. 105974, 2022.

[18] I. Yousef, V. Morozov, V. Sudakov, and I. Idrisov, "Cementation characteristics and their effect on quality of the upper triassic, the lower cretaceous, and the upper cretaceous sandstone reservoirs, euphrates graben, Syria," *Journal of Earth Science*, vol. 32, no. 6, pp. 1545–1562, 2021.

[19] Q. Xu, X. Xie, C. Zhang, L. Hai, A. Busbey, and V. Heesakkers, "Integrated diagenesis study of tight gas sandstone: the permian lower shihezi formation, northern Ordos Basin, China," *Lithosphere*, vol. 2022, no. 1, 2022.

[20] B. Jiu, W. Huang, Y. Li, and M. He, "Influence of clay minerals and cementation on pore throat of tight sandstone gas reservoir in the eastern Ordos Basin, China," *Journal of Natural Gas Science and Engineering*, vol. 87, March, p. 103762, 2021.

[21] G. Desbois, J. L. Urai, P. A. Kukla, J. Konstanty, and C. Baerle, "High-resolution 3D fabric and porosity model in a tight gas sandstone reservoir: A new approach to investigate microstructures from mm- to nm-scale combining argon beam cross-sectioning and SEM imaging," *Journal of Petroleum Science and Engineering*, vol. 78, no. 2, pp. 243–257, 2011.

[22] R. Rezaee, A. Saeedi, and B. Clennell, "Tight gas sands permeability estimation from mercury injection capillary pressure and nuclear magnetic resonance data," *Journal of Petroleum Science and Engineering*, vols. 88–89, June, pp. 92–99, 2012.

[23] A. A. Hinai, R. Rezaee, L. Esteban, and M. Labani, "Comparisons of pore size distribution: A case from the western australian gas shale formations," *Journal of Unconventional Oil and Gas Resources*, vol. 8, December, pp. 1–13, 2014.

[24] A. S. Ziarani and R. Aguilera, "Pore-throat radius and tortuosity estimation from formation resistivity data for tight-gas sandstone reservoirs," *Journal of Applied Geophysics*, vol. 83, August, pp. 65–73, 2012.

[25] B. Bai, R. Zhu, S. Wu, et al., "Multi-scale method of nano(micro)-CT study on microscopic pore structure of tight sandstone of yanchang formation, Ordos Basin," *Petroleum Exploration and Development*, vol. 40, no. 3, pp. 354–358, 2013.

[26] L. Min, T. Zheng-wu, L. Quan-wen, et al., "A new method for obtaining the rock pore structure eigenvalue," *Journal of Natural Gas Science and Engineering*, vol. 22, January, pp. 478–482, 2015.

[27] R. G. Loucks, R. M. Reed, S. C. Ruppel, and D. M. Jarvie, "Morphology, genesis, and distribution of nanometer-scale pores in siliceous mudstones of the mississippian barnett shale," *Journal of Sedimentary Research*, vol. 79, no. 12, pp. 848–861, 2009.

[28] D. P. Edward, "Relationship of porosity and permeability to various parameters derived from mercury injection-capillary pressure curves for sandstone (1)," *AAPG Bulletin*, vol. 76, pp. 191–198, 1992.

[29] C. R. Clarkson, N. Solano, R. M. Bustin, et al., "Pore structure characterization of north American shale gas reservoirs using USANS/SANS, gas adsorption, and mercury intrusion," *Fuel*, vol. 103, January, pp. 606–616, 2013.

[30] D. Xiao, S. Lu, J. Yang, L. Zhang, and B. Li, "Classifying multiscale pores and investigating their relationship with porosity and permeability in tight sandstone gas reservoirs," *Energy & Fuels*, vol. 31, no. 9, pp. 9188–9200, 2017.

[31] N. Alyafei, T. J. Mckay, and T. I. Solling, "Characterization of petrophysical properties using pore-network and lattice-boltzmann modelling: Choice of method and image sub-volume size," *Journal of Petroleum Science and Engineering*, vol. 145, September, pp. 256–265, 2016.

[32] Y. Yao, D. Liu, Y. Che, D. Tang, S. Tang, and W. Huang, "Non-destructive characterization of coal samples from China using microfocus X-ray computed tomography," *International Journal of Coal Geology*, vol. 80, no. 2, pp. 113–123, 2009.

[33] H. Wu, Y. Ji, R. Liu, C. Zhang, and S. Chen, "Insight into the pore structure of tight gas sandstones: A case study in the Ordos Basin, NW China," *Energy & Fuels*, vol. 31, no. 12, pp. 13159–13178, 2017.

[34] B. F. Swanson, "A simple correlation between permeabilities and mercury capillary pressures," *Journal of Petroleum Technology*, vol. 33, no. 12, pp. 2498–2504, 1981.

[35] M. H. H. Mohammadlou and M. B. B. Mørk, "Integrated permeability analysis in tight and brecciated carbonate reservoir," *SPE Reservoir Evaluation & Engineering*, vol. 15, no. 6, pp. 624–635, 2012.

[36] H. A. Nooruddin, M. E. Hossain, H. Al-Yousef, and T. Okasha, "Comparison of permeability models using mercury injection capillary pressure data on carbonate rock samples," *Journal of Petroleum Science and Engineering*, vol. 121, September, pp. 9–22, 2014.

[37] J. S. Kolodzie, "Analysis of pore-throat size and use of the waxman–smits equation to determine OOIP in spindle field, colorado," in *Presented at SPE 55th Annual Technical Conference and Exhibition. Paper 9382*, pp. 21–24, Dallas, TX, n.d.

[38] M. R. Rezaee, A. Jafari, and E. Kazemzadeh, "Relationships between permeability, porosity and pore throat size in carbonate rocks using regression analysis and neural networks," *Journal of Geophysics and Engineering*, vol. 3, no. 4, pp. 370–376, 2006.

[39] Z. Guo, J. Zhang, and Z. Yu, "The evolutional characteristics of structure of the oil and gas bearing areas in ordos massif," *Pet Explor Dev*, vol. 21, pp. 22–29, 1994.

[40] Z. X. He, *The Tectonic Evolvement and Petroleum in the Ordos Basin*, Petroleum Industry Press, Beijing, 2002.

[41] Q. Xu, W. Shi, X. Xie, et al., "Inversion and propagation of the late paleozoic porjianghaizi fault (north Ordos Basin, China): Controls on sedimentation and gas accumulations," *Marine and Petroleum Geology*, vol. 91, March, pp. 706–722, 2018.

[42] Y. Yang, W. Li, and L. Ma, "Tectonic and stratigraphic controls of hydrocarbon systems in the ordos basin: A multicycle cratonic basin in central China," *AAPG Bulletin*, vol. 89, no. 2, pp. 255–269, 2005.

[43] H. Yang, J. Fu, X. Wei, and X. Liu, "Sulige field in the ordos basin: Geological setting, field discovery and tight gas reservoirs," *Marine and Petroleum Geology*, vol. 25, nos. 4–5, pp. 387–400, 2008.

[44] S. Huang, X. Fang, D. Liu, C. Fang, and T. Huang, "Natural gas genesis and sources in the zizhou gas field, Ordos Basin, China," *International Journal of Coal Geology*, vol. 152, November, pp. 132–143, 2015.

[45] Q. Liu, Z. Jin, Q. Meng, X. Wu, and H. Jia, "Genetic types of natural gas and filling patterns in daniudi gas field, Ordos Basin, China," *Journal of Asian Earth Sciences*, vol. 107, August, pp. 1–11, 2015.

[46] K. Liu, R. Wang, W. Shi, et al, "Tectonic controls on permian tight gas accumulation: Constrains from fluid inclusion and paleo-structure reconstruction in the Hangjinqi area, northern Ordos Basin, China," *Journal of Natural Gas Science and Engineering*, vol. 83, November, p. 103616, 2020.

[47] S. Qin, R. Wang, W. Shi, et al, "Diverse effects of intragranular fractures on reservoir properties, diagenesis, and gas migration: Insight from permian tight sandstone in the Hangjinqi area, north Ordos Basin," *Marine and Petroleum Geology*, vol. 137, March, p. 105526, 2022.

[48] R. Wang, W. Shi, X. Xie, et al, "Clay mineral content, type, and their effects on pore throat structure and reservoir properties: Insight from the permian tight sandstones in the hangjinqi area, north Ordos Basin, China," *Marine and Petroleum Geology*, vol. 115, May, p. 104281, 2020.

[49] R. Wang, K. Liu, and W. Shi, "Reservoir densification, pressure evolution, and natural gas accumulation in the upper paleozoic tight sandstones in the north Ordos Basin, China," *Energies*, vol. 15, no. 6, p. 1990, 1990.

[50] M. Yang, L. Li, J. Zhou, et al., "Mesozoic structural evolution of the hangjinqi area in the northern Ordos Basin, north China," *Marine and Petroleum Geology*, vol. 66, September, pp. 695–710, 2015.

[51] E. W. Washburn, "The dynamics of capillary flow," *Physical Review*, vol. 17, no. 3, pp. 273–283, 1921.

[52] R. L. Folk, *Petrology of Sedimentary Rocks*, Hemphill Publishing, Austin, Texas, 1980.

[53] J. Wang, S. Wu, Q. Li, J. Zhang, and Q. Guo, "Characterization of the pore-throat size of tight oil reservoirs and its control on reservoir physical properties: A case study of the triassic tight sandstone of the sediment gravity flow in the

Ordos Basin, China," *Journal of Petroleum Science and Engineering*, vol. 186, March, p. 106701, 2020.

[54] D. Zhao, J. Hou, H. Sarma, et al., "Pore throat heterogeneity of different lithofacies and diagenetic effects in gravelly braided river deposits: Implications for understanding the formation process of high-quality reservoirs," *Journal of Petroleum Science and Engineering*, vol. 221, 2023.

[55] R. G. Loucks, R. M. Reed, S. C. Ruppel, and U. Hammes, "Spectrum of pore types and networks in mudrocks and a descriptive classification for matrix-related mudrock pores," *AAPG Bulletin*, vol. 96, no. 6, pp. 1071–1098, 2012.